

---

# CMS Physics Analysis Summary

---

Contact: cms-pag-conveners-sus@cern.ch

2025/04/07

## Search for compressed electroweakinos with low-momentum isolated tracks

The CMS Collaboration

### Abstract

A search is presented for higgsino dark matter (DM) in final states with a low momentum (soft), isolated track and large missing transverse momentum. In the minimal supersymmetric standard model (MSSM), charginos are most often produced in association with a nearly mass-degenerate neutralino or another chargino, and predominantly decay into the lightest neutralino (DM candidate) and a soft pion. For a mass difference  $\Delta m^\pm$  less than 1 GeV, a discernible displacement of the pion's track with respect to the primary vertex can arise, reaching up to about 1 cm for the smallest allowed  $\Delta m^\pm$ . A parameterized multivariate classifier is employed to distinguish the signal track from background tracks, optimally targeting a range of  $\Delta m^\pm$  by exploiting the track transverse momentum, impact parameter, and event topology to varying degrees depending on the assumed  $\Delta m^\pm$ . The analyzed data correspond to an integrated luminosity of  $138 \text{ fb}^{-1}$  collected by the CMS experiment in proton-proton collisions at  $\sqrt{s} = 13 \text{ TeV}$ . No evidence of new physics is observed, and limits are set at the 95% confidence level in the mass plane of the model. Assuming MSSM cross sections, values of  $\Delta m^\pm$  between 0.28 and 1.15 GeV are excluded for a 100 GeV mass chargino, and chargino masses up to 185 GeV are excluded for  $\Delta m^\pm$  of 0.55 GeV.



## 1 Introduction

Weak-scale supersymmetry (SUSY) [1–9] is a well motivated framework for physics beyond the standard model (BSM) that addresses a number of gaps in current understanding. It provides a possible explanation for dark matter (DM) [10, 11], resolves the large hierarchy problem [12], and renders Grand Unification more straightforward. The simplest realizable SUSY model, the R-parity conserving minimal supersymmetric standard model (MSSM) [13], is highly constrained by the DM relic density [14], collider experiments [15] [16], and direct detection experiments [17–19]. However, distinct theory phase space remains viable [20], with a noteworthy region of parameter space featuring light Higgs boson superpartners, called higgsinos. Such scenarios additionally solve the so-called little Hierarchy problem [13], whereby fine-tuning among the MSSM parameters is required to predict a light SM electroweak sector.

Higgsino DM is the lightest state  $\tilde{\chi}_1^0$  of four nearly-degenerate electroweakinos, the others being  $\tilde{\chi}_2^0$ , and  $\tilde{\chi}_1^\pm$ , with mass differences  $\Delta m^\pm \equiv m(\tilde{\chi}_1^\pm) - m(\tilde{\chi}_1^0)$  and  $\Delta m^0 \equiv m(\tilde{\chi}_2^0) - m(\tilde{\chi}_1^0)$  of order 1 GeV or less. Radiative corrections [21] give rise to a minimum mass splitting  $\Delta m^\pm$ , establishing a lower limit of approximately 0.25 GeV for  $m(\tilde{\chi}_1^0) = 100$  GeV and gradually increasing with larger LSP mass. The optimal analysis strategy depends on the mass differences. When  $\Delta m^0$  is larger than 1 GeV soft, prompt leptons from the decay of the electroweakinos are sensitive probes [22, 23]. If  $\Delta m^\pm$  is smaller than  $\approx 0.3$  GeV, the chargino length becomes large—several cm—such that it reaches the tracking detector before decaying, giving rise to a disappearing track signature [24–26]. The intermediate region,  $0.3 \text{ GeV} \lesssim \Delta m^\pm \lesssim 1 \text{ GeV}$ , is difficult to probe with either of those methods, as leptons are prohibitively soft and charginos that are not sufficiently long-lived to record a track. The most probable decay mode thus can give rise to mildly-displaced, low-momentum hadrons, usually a single pion. By exploiting the track’s isolation,  $p_T$ , and displacement w.r.t. the PV, as well as the event topology allows sensitivity in the intermediate region [21, 27]. The production processes are shown in Fig. 1.

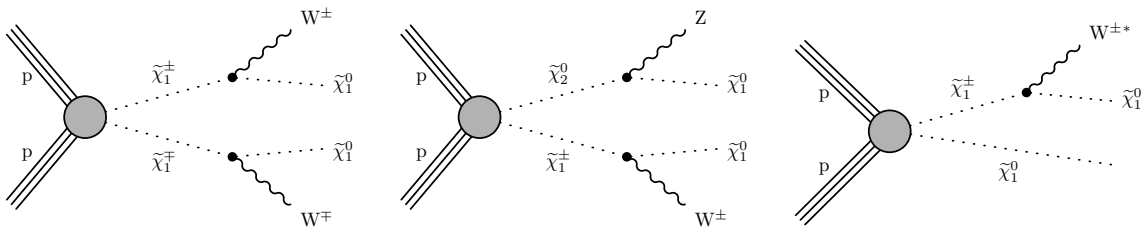


Figure 1: Feynman diagrams for electroweakino pair production.

We present an analysis of the signature of soft and slightly displaced tracks, targeting chargino decays in scenarios with  $\Delta m^\pm$  between 0.3 and 1 GeV. Events are selected with online (offline) missing transverse momentum  $p_T^{\text{miss}}$  greater than 120 (300) GeV, at least one isolated track, and no isolated electrons, muons, or photons. To maximize the reach of the search, a parametrized neural network (NN) classifier is employed to distinguish signal tracks from a large rate of background tracks, taking as input track and event kinematic information, observables related to the track’s displacement, as well as the model parameter  $\Delta m^\pm$ . A cut-based based analysis based on similar observables was previously reported by ATLAS [27].

## 2 CMS detector, reconstruction, and simulation

The CMS detector is structured around a cylindrical superconducting solenoid with an inner diameter of 6 m. The solenoid provides a nearly uniform 3.8 T magnetic field within its vol-

ume. The innermost detectors are silicon pixel and strip tracking detectors, followed by a lead tungstate crystal electromagnetic calorimeter (ECAL), and a brass and scintillator hadron calorimeter (HCAL), surrounded by the solenoid. Muons are measured with gas-ionization detectors embedded in a steel flux-return yoke outside the solenoid, allowing muon reconstruction within  $|\eta| < 2.4$ . The CMS components taken together provide a nearly hermetic detector, allowing for accurate measurements of  $p_T^{\text{miss}}$ . A detailed description is given in Ref. [16].

The tracking detector consists of an inner pixel detector and an outer strip detector. The tracker used for the 2016 data-taking period, referred to as the “Phase-0” tracker, measured particles within  $|\eta| < 2.5$ . At the beginning of 2017, an upgraded pixel detector was installed [28]. The upgraded tracker is referred to as the “Phase-1” tracker. The Phase-1 tracker measured particles within  $|\eta| < 3.0$ . Tracks traversing the tracker system encounter 3 (4) pixel layers within a radius of 102 (160) mm in the Phase-0 (Phase-1) tracker. The Phase-1 tracker provides improved tracking and vertex resolution, and enhanced b-tagging performance.

Individual particles are reconstructed as particle-flow (PF) objects with the CMS PF algorithm [29], which identifies them as photons, charged hadrons, neutral hadrons, electrons, or muons. The primary vertex (PV) is taken to be the vertex corresponding to the hardest scattering in the event, evaluated using tracking information alone as described in Section 9.4.1 of Ref. [30]. Charged-particle tracks associated with vertices other than the PV are removed from further consideration. Jets are defined by clustering PF candidates using the anti- $k_T$  jet algorithm [31, 32] with a distance parameter of 0.4. Jet quality criteria [33, 34] are imposed to eliminate jets from spurious sources such as electronics noise. Jet energies are corrected for the nonlinear response of the detector [35] and to account for contributions of particles from simultaneous pp interactions (pileup) [36]. Jets arising from the hadronization of b-quarks, b jets, are identified by the combined secondary vertex algorithm based on deep NNs, DEEPCSV [37], with a high efficiency of around 80%.

The SM production of  $t\bar{t}$ , W+jets, and Z+jets events is simulated at leading order (LO) precision using the MADGRAPH5.aMC@NLO 2.2.2 [38, 39] event generator with up to four additional partons. The simulation of the detector response is based on the GEANT4 [40] application. For background events, the Phase-0 samples use the CUETP8M1 [41] tune while the Phase-1 samples use the CP5 [42] tune. Simulated samples generated at LO (NLO) with the CUETP8M1 tune use the NNPDF3.0LO (NNPDF3.0NLO) [43] parton distribution function (PDF). Those generated with the CP2 or CP5 tune use the NNPDF3.1LO (NNPDF3.1NNLO) [44] PDF. Additional pp collisions within the same or adjacent bunch crossings (pileup) are generated as inelastic collisions using PYTHIA 8.240. Simulated events are weighted to reproduce the distribution of the number of interactions observed in data.

Signal events are generated at LO using the PYTHIA 8.240 generator [45] with the detector response based on the CMS fast simulation program [46, 47]. FastSim observables have been compared with the full GEANT4-based simulation for consistency and corrected as appropriate. Parton showering and hadronization are simulated with the PYTHIA 8.205 generator [45]. We consider a scenario corresponding to large values of  $\tan\beta$  [21], which gives rise to the relation  $\Delta m^0 = 2\Delta m^\pm$ . Decays of the chargino and branching fractions are calculated in [48], where for small  $\Delta m^\pm$ , the dominant decay of the chargino  $\tilde{\chi}_1^\pm$  is to the LSP and a single pion. As  $\Delta m^\pm$  increases, other decay modes, in particular the two-pion mode increases and surpasses the single pion mode for values of  $\Delta m^\pm$  greater than 800 MeV.

### 3 Object and event selection

Signal candidate tracks are selected with  $p_T < 20$  GeV and  $|\eta| < 2.4$ . No lower  $p_T$  threshold is applied on tracks at the analysis level, and the reconstruction retains 10% efficiency for  $p_T$  as low as 100 MeV, increasing to 80% by 500 MeV and 90% by 1 GeV. Criteria are placed on the goodness of fit and the number of reconstructed hits associated to tracks to ensure high purity of charged particles. Tracks are required to be isolated from jets with  $p_T > 30$  GeV, satisfying  $\Delta R(\text{track}, \text{jet}) > 0.4$ .

Jets are selected to have  $p_T > 30$  GeV and  $|\eta| < 5$ . Additional criteria are placed on the fractions of jet energy associated with charged and neutral particles in the ECAL and HCAL to suppress jets arising from detector noise and pileup interactions, with negligible loss in signal efficiency. Hadronic  $\tau$  candidates are selected from a superset of jets with  $p_T > 20$  GeV and  $|\eta| < 2.3$  using track, vertex, and calorimetric information to increase purity.

Electrons and photons are selected with  $|\eta| < 2.5$ ,  $p_T > 10$  and 15 GeV, respectively. Selection on the shower shape, calorimetric energy, and track measurements is made for an optimal compromise of efficiency and purity. Muons, selected with high efficiency, are required to have  $p_T > 10$  GeV and  $|\eta| < 2.4$ , with a consistent trajectory measured by the inner and outer tracking systems. Electrons, photons and muons are further required to satisfy relative isolation, where the sum of  $p_T$  of reconstructed particles within a small  $\Delta R$  of the given object is less than 20% of the object's value

The  $p_T^{\text{miss}}$  is computed as the negative vectorial sum of the transverse momenta of all reconstructed particle flow candidates. An alternate construction  $H_T^{\text{miss}}$ , defined as the magnitude of the vector sum of the transverse momenta of all jets with  $p_T > 30$  GeV and  $|\eta| < 5.0$ , is also used to render the offline selection more consistent with the analysis trigger; both measures are corrected to mitigate effects of pileup and geometric dependencies of jet energy scale and resolution. Finally, the scalar sum of the transverse momenta of all jets with  $p_T > 30$  GeV and  $|\eta| < \eta^{\text{cut}}$  ( $H_T^{\eta^{\text{cut}}}$ ) is used to remove events with spurious jets in the forward region.

Events are selected which pass standard filters that remove events with anomalously large  $p_T^{\text{miss}}$  arising from calorimeter noise, mis-reconstructed particles and vertices, and beam halo interactions in the detector [49]. These filters have a negligible impact on the signal selection efficiency and generally bring data and simulation into better agreement. Events with abnormally large energy deposits in the forward region are discarded by requiring  $H_T(|\eta_{\text{jet}}| < 5)/H_T(|\eta_{\text{jet}}| < 2.4) < 2$ . To mitigate the influence of the outage of two sectors of the hadronic endcap calorimeter in the 2018 data taking period ("HEM 15/16 failure"), events in the 2018 era are vetoed if there is a jet present that fulfills  $p_T > 30$  GeV,  $\Delta\phi(\text{jet}, \vec{H}_T^{\text{miss}}) < 0.5$ ,  $\eta \in [-3.2, -1.2]$ ,  $\varphi \in [-1.77, -0.67]$ . The event baseline selection criteria are listed in Table 1.

#### 3.1 Track classifier and signal regions

A multi-class NN classifier parameterized in  $\Delta m^\pm$  is used to distinguish potential signal tracks from background tracks. To train the network, simulated and reconstructed tracks are geometrically matched to detector-stable generator particles to form categories for the training and validation samples. The signal training samples include a range of masses and  $\Delta m^\pm$  values spanning the target region of the analysis, and background events are simulated SM processes that contribute to the SRs. To ensure high sensitivity over the range of model phase space, samples are weighted to be uniform in  $\Delta m^\pm$  and  $m(\tilde{\chi}_1^\pm)$ . Tracks matched to generator pions linked to chargino decay make up the signal class. Tracks taken from simulated  $Z \rightarrow \nu\nu$  and  $W \rightarrow \ell\nu$  events matched to prompt and secondary particles are each assigned to a background

Table 1: The analysis baseline selection criteria.

Observable	Cut value
$p_T^{\text{miss}}$	$> 300 \text{ GeV}$
$N_{\text{jet}}(p_T > 100 \text{ GeV})$	$\geq 1$
$H_T^{\text{miss}}$	$> 300 \text{ GeV}$
$\Delta\varphi_{\text{min}}(\vec{p}_T^{\text{miss}}, \text{jet}_{1,2,3,4})$	$> 0.5$
$N_{\text{jet}}(p_T > 30 \text{ GeV})$	$< 5$
$N_{\text{jet}}(p_T > 30 \text{ GeV}, \text{b-tagged})$	$= 0$
$N_{\text{isolated photon}}$	$= 0$
$N_{\text{isolated electron}}$	$= 0$
$N_{\text{isolated muon}}$	$= 0$
$N_{\tau}$	$= 0$

class, as are tracks associated with secondary decay products from  $W \rightarrow \tau\nu$  events. Finally, tracks without any associated generator particle define a fourth background class referred to as spurious tracks. Background tracks are weighted by production cross section and randomly assigned  $\Delta m^\pm$  values from a uniform distribution. The data set is divided into a train and a test subset.

Selected characteristics of signal tracks are shown in Fig. 2, and vary depending on the signal model parameter  $\Delta m^\pm$ . The  $p_T$  of the signal tracks peaks around the scale of  $\Delta m^\pm$ , as seen in the upper left, while the displacement of the signal track increases with smaller  $\Delta m^\pm$ , as seen in the upper right. The impact parameter (IP) significance follows a bimodal distribution for background; one peak at small values corresponding to tracks from the PV and another peak at higher values comprising "spurious" tracks, a category that includes both pileup and fake tracks. Signal tracks are isolated from jets (lower left) and point more in the direction of  $\vec{p}_T^{\text{miss}}$  than do background tracks (lower right). Variants on the IP significance corresponding to pileup vertices, as well as the vertex associated with the track during reconstruction, are all included as input. Certain systematic differences between data and simulation are observed, such as the spectrum of  $p_T$ , which can result from mis-modeling of track momentum scale, resolution, tracker alignment, and the underlying spectrum of soft charged particles.

The NN is parameterized by the mass splitting  $\Delta m^\pm$  in order to exploit properties of tracks and their correlations, which change depending on the model phase space. To account for different characteristics of tracks from different classes, the network has five output nodes, one for signal tracks and one for each of the four background classes: PV-associated (prompt and secondary), spurious, and  $\tau$  tracks. The NN is trained to be calibrated, meaning its output is an estimator of the likelihood of the track being of a given category. The NN uses the 37 variables listed in Table 3 in the Appendix, as well as a one-hot encoded variable encoding the year of data taking, which correspond to different physical tracking detectors and pileup conditions. The logit transform, denoted by tilde-hat and defined as

$$\tilde{P} \equiv \text{logit}(P) = \ln\left(\frac{P + \epsilon}{1 - P + \epsilon}\right), \quad \epsilon = 1 \times 10^{-6} \quad (1)$$

is applied to the output nodes to enhance the resolution in the region of high likelihood.

Signal regions (SRs) are defined by computing the maximum-scoring track, considering all tracks in a given event and the three  $\Delta m^\pm$  values, 0.3, 0.6, and 1.0 GeV. Depending on which

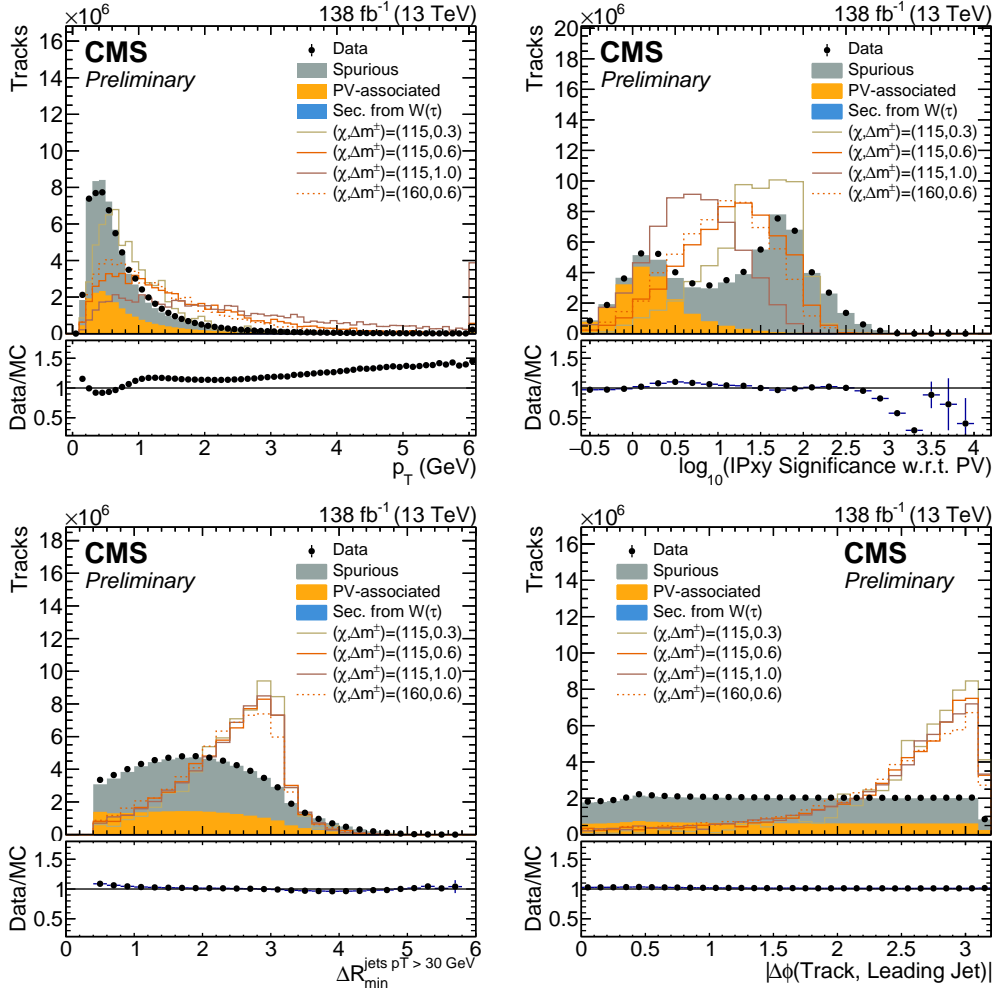


Figure 2: Distributions of kinematic track observables for background tracks and signal tracks from four example signal model points. The filled histograms show distributions for background tracks in SM background events, normalized to the integral of the total background. Shown as lines are distributions of chargino-matched tracks in signal events for selected benchmark models.

value of  $\Delta m^\pm$  is associated with the maximum scoring track, the event is sorted into a corresponding category and characterized by the maximum logit-transformed score  $\tilde{P}_{\max}$ . This construction ensures non-overlapping categories and therefore disjoint SRs. A final binning in each category, optimized for analysis sensitivity, leads to the 12 SRs. The bin boundaries are given in Section 5.

## 4 Background estimation

The backgrounds stem from SM events with significant  $p_T^{\text{miss}}$  in which soft tracks fake the signature of the signal pion. The expected background event yields are estimated using templates for each track category, derived in simulation that has been corrected using data. While the dominant contribution of events arises from  $Z \rightarrow \nu\nu$  and  $W \rightarrow \ell\nu$  processes, the tracks mainly stem from the underlying event, pileup interactions, and errors in the reconstruction (fakes), and are therefore largely independent of the hard process. The data-based MC corrections are derived in a Drell-Yan (DY) data set described in the following subsection, followed by a

description of the corrections and a discussion of the validation.

#### 4.1 Cleaned Drell-Yan CR

To get a well-controlled sample that represents the main SM background process  $Z \rightarrow \nu\nu$ , a sample of  $Z \rightarrow \mu\mu$  events is selected and the muons “removed” from the event record to mimic neutrinos. The resulting sample is referred to as the cleaned Drell-Yan sample. The event observables such as  $p_T^{\text{miss}}$  are re-computed in this sample, yielding a good proxy of  $Z \rightarrow \nu\nu$  events. Notably, the soft component of the event, the track-level background, is not directly affected by the cleaning.

The cleaned Drell-Yan sample is constructed by first selecting events with two oppositely charged, isolated muons, each with  $p_T(\mu) > 30 \text{ GeV}$  and relative isolation less than 0.2. The muon pair is required to be consistent with Z boson decay products by having an invariant mass of the  $\mu\mu$  system in the range  $m_Z \in (75, 105]$ , and to have system  $p_T(Z)$  exceeding 200 GeV. The transverse momenta of the selected muons are vectorially added to the  $p_T^{\text{miss}}$  and the muons and matching tracks, PF candidates, photons, and jets are removed from the event record. The matching is done using an angular  $\Delta R$  criterion with thresholds of 0.4 for the jet matching and 0.05 for all other objects. This cleaning is performed in real and simulated event samples, and the simulated cleaned DY events are reweighted based on the  $p_T$  of the generator Z boson to match with that in the  $Z \rightarrow \nu\nu$  sample.

#### 4.2 Corrections to simulated events

The overall rates of the PV-associated and spurious track classes in simulation are corrected by the application of normalization factors (scale factors) derived from the comparison of simulation and data for different values of the longitudinal impact parameter of candidate tracks. By requiring  $dz$  with respect to the PV less than 0.001 cm for PV-associated tracks and greater than 0.63 cm for spurious tracks the scale factors and their statistical uncertainty are determined to be 0.9116 for PV-associated and 1.18 for spurious tracks.

Potential mis-modeling in the shape of  $\tilde{P}_{\text{max}}(\text{Signal} | \Delta m = 0.3, 0.6, 1.0 \text{ GeV})$ , due to the estimated uncertainty in track impact parameters and the  $p_T$  of soft tracks is corrected using a multivariate regression. A neural network is trained and employed to morph simulated observables to better agree with real data. For the training, inclusive sets of tracks passing the preselection are taken from the cleaned DY CR in data and MC. The regression NN outputs refined values of these observables, minimizing the maximum mean discrepancy (MMD) [50] loss evaluated between the training data and refined simulation. This technique is based on the Fast Perfekt methodology [51], and more details are provided in the Appendix. The results of the refinement applied to the three variables are shown in Fig. 3 (upper), as well as for the three signal node scores (lower), having propagated the refined inputs through the classifier. The procedure leads to improved modeling of simulated tracks, particularly for PV-associated and  $\tau$  tracks, and is applied to all simulated tracks. Some features retain a larger discrepancies, but not in regions relevant for the SRs.

Background MC samples are corrected to improve the agreement with the  $p_T^{\text{miss}}$  distribution observed in data. For this, a line fit is performed to events passing the event selection (but no cut on the signal node scores) in the region  $300 \text{ GeV} < p_T^{\text{miss}} < 1000 \text{ GeV}$  and simulated events are reweighted according to the corresponding function value. Events with  $p_T^{\text{miss}} > 1000 \text{ GeV}$  are weighted with the value at  $p_T^{\text{miss}} = 1000 \text{ GeV}$ .

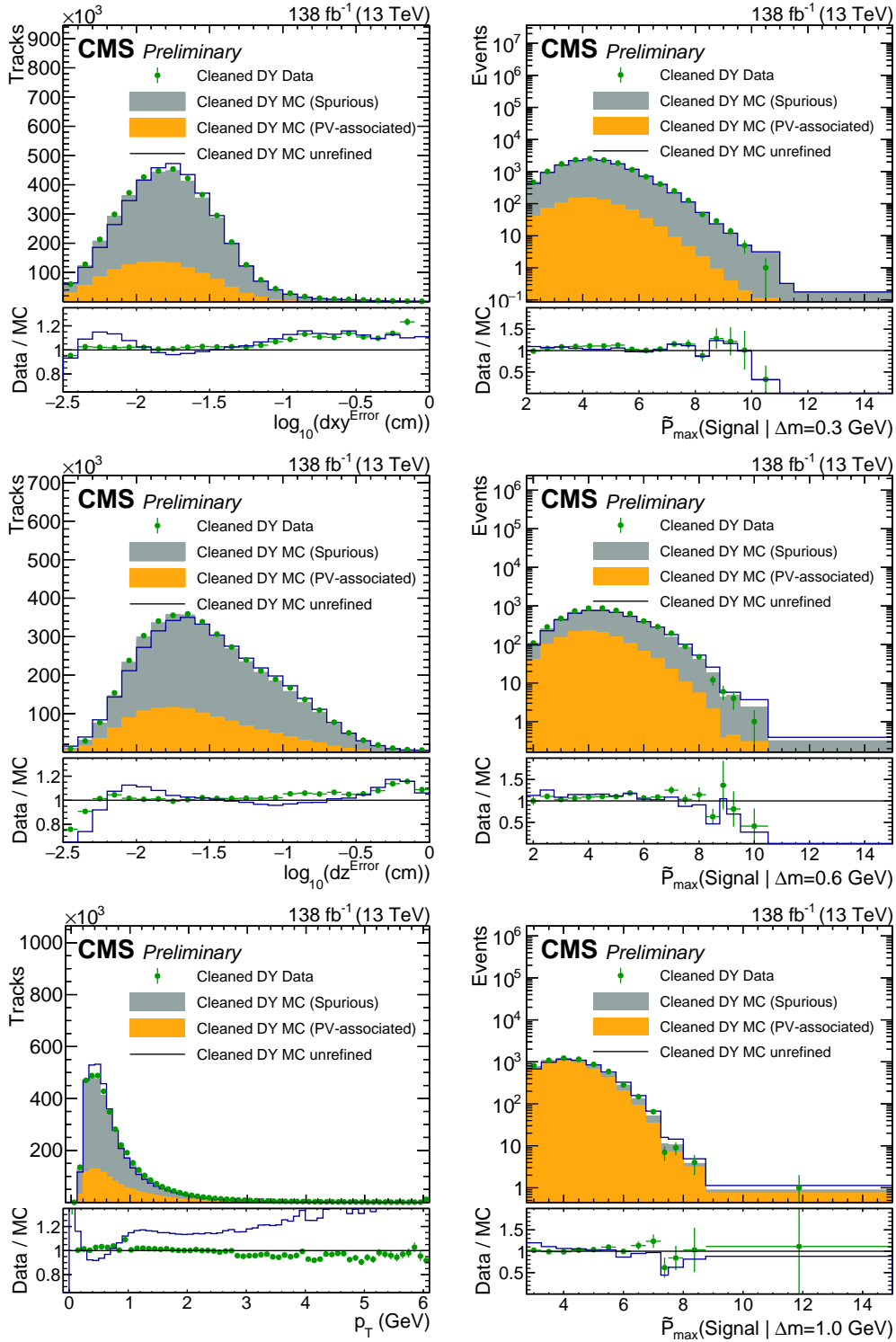


Figure 3: Left: distributions of the three track variables subject to refinement. The distributions for data are shown alongside those for (unrefined) MC. Right: distributions of  $\tilde{P}_{max}(\text{Signal} | \Delta m = 0.3 \text{ GeV})$ ,  $\tilde{P}_{max}(\text{Signal} | \Delta m = 0.6 \text{ GeV})$ , and  $\tilde{P}_{max}(\text{Signal} | \Delta m = 1.0 \text{ GeV})$  for events in data as well as in MC with and without refinement applied to the input variables.

Table 2: Expected and observed yields in the 12 SRs with a breakdown of the background components and three benchmark signal models, as well as the definitions of the SRs based on the bin boundaries in the range of  $\tilde{P}_{\max}(\text{Signal} | \Delta m = 0.3, 0.6, 1.0 \text{ GeV})$ . Uncertainties are statistical only.

Signal regions		Background					Signal [ $m(\tilde{\chi}_1^\pm), \Delta m^\pm$ ] (GeV)				
$\Delta m^*$	Bin	$\tilde{P}_{\max}$	PV	Spurious	$W \rightarrow \tau\nu$	Tot	Data	[115, 0.268]	[115, 0.568]	[115, 0.968]	
0.3	1	9.5-10	$1.03 \pm 0.21$	$29.9 \pm 1.2$	$0.14 \pm 0.06$	$31.0 \pm 1.2$	31	$3.63 \pm 0.62$	$3.34 \pm 0.75$	$0.44 \pm 0.30$	
	2	10-11	$0.65 \pm 0.19$	$19.3 \pm 0.9$	$0.14 \pm 0.06$	$20.1 \pm 0.9$	10	$2.62 \pm 0.54$	$5.87 \pm 1.09$	$1.04 \pm 0.51$	
	3	11-11	$0.03 \pm 0.03$	$1.80 \pm 0.22$	$0.03 \pm 0.02$	$1.86 \pm 0.22$	3	$0.24 \pm 0.15$	$0.57 \pm 0.26$	$0.26 \pm 0.24$	
	4	11.5- $\infty$	$0.02 \pm 0.03$	$0.84 \pm 0.16$	-	$0.87 \pm 0.16$	1	$2.40 \pm 0.03$	$3.66 \pm 0.05$	$1.92 \pm 0.03$	
0.6	5	8.75-9	$3.72 \pm 0.56$	$36.1 \pm 1.8$	$0.88 \pm 0.34$	$40.7 \pm 1.9$	41	$2.53 \pm 0.56$	$19.9 \pm 2.1$	$1.88 \pm 0.64$	
	6	9-9.5	$4.03 \pm 0.64$	$34.4 \pm 1.7$	$0.57 \pm 0.13$	$39.0 \pm 1.8$	34	$1.89 \pm 0.35$	$19.1 \pm 1.8$	$2.15 \pm 0.55$	
	7	9.5-10.5	$1.33 \pm 0.22$	$15.4 \pm 0.9$	$0.28 \pm 0.08$	$17.0 \pm 0.9$	15	$1.86 \pm 0.43$	$15.9 \pm 1.8$	$1.33 \pm 0.43$	
	8	10.5- $\infty$	$0.27 \pm 0.12$	$1.48 \pm 0.24$	$0.07 \pm 0.04$	$1.82 \pm 0.27$	3	$0.40 \pm 0.18$	$2.93 \pm 0.82$	$0.77 \pm 0.41$	
1.0	9	7.5-7.25	$56.2 \pm 2.1$	$36.0 \pm 2.0$	$14.9 \pm 1.9$	$107 \pm 3$	109	$2.60 \pm 0.44$	$15.9 \pm 1.5$	$16.6 \pm 1.5$	
	10	7.5-8	$48.9 \pm 2.0$	$26.8 \pm 1.5$	$10.9 \pm 1.2$	$86.6 \pm 2.7$	74	$2.21 \pm 0.35$	$16.9 \pm 1.6$	$17.0 \pm 1.4$	
	11	8-8.75	$17.1 \pm 0.8$	$6.14 \pm 0.59$	$3.87 \pm 0.46$	$27.1 \pm 1.1$	30	$1.72 \pm 0.39$	$9.26 \pm 1.14$	$7.20 \pm 0.93$	
	12	8.75- $\infty$	$3.12 \pm 0.30$	$0.67 \pm 0.13$	$1.13 \pm 0.11$	$4.92 \pm 0.34$	8	$0.58 \pm 0.20$	$2.20 \pm 0.59$	$3.34 \pm 0.73$	

## 5 Results and interpretation

The expected and observed distributions for the  $\tilde{P}_{\max}(\text{Signal} | \Delta m = \{0.3, 0.6, 1.0\} \text{ GeV})$  observables are shown in Fig. 4, and in the 12 SRs in Fig. 5 (left). The yields are tabulated in Table 2. No significant excess of data over the expectation is observed that would constitute evidence of new physics. The data are interpreted in terms of a maximum likelihood fit, accounting for the background and signal modeling along with various sources of systematic uncertainty.

Uncertainty in the scale factors for the PV-associated and spurious backgrounds to account for potential possible bias in the relative rates due to the max score criterion applied to tracks within each event is assessed at approximately 10%. Uncertainty in the MC shape, corrected by the refinement, is evaluated by fitting polynomials to the ratio of data to refined MC in the signal-sensitive regions  $\tilde{P}_{\max}(\text{Signal} | \Delta m = \{0.3, 0.6, 1.0\} \text{ GeV}) > 5$  of the cleaned DY CR and varies up to 10%, depending on the SR. Other systematic uncertainties are applied to simulated events to account for potential mis-modeling of the jet energy, pileup, and inefficiencies in the trigger. A small uncertainty of 1.6% in the luminosity assessed for Run 2 based on [52–55]. An overall uncertainty is assessed for the modeling of signal events based on the agreement between data and simulation in a  $\tau$ -enriched CR, amounting to 10%, as well as large uncertainties ranging up to 80% to cover possible modeling effects of the fast simulation. Systematic (statistical) uncertainties are encoded in the likelihood using Gamma (log-normal) functions with a width set by the respective estimate of the systematic uncertainty.

Limits are derived based on  $\text{CL}_s$  asymptotic approximation; the expected and observed limits are shown in Fig. 5 (right) in the mass plane of the electroweakinos. The excluded region encompasses  $\Delta m^\pm \in [0.33, 1.1] \text{ GeV}$  for  $m(\tilde{\chi}_1^\pm) = 100 \text{ GeV}$  and extends to around 185 GeV for  $\Delta m^\pm = 0.55 \text{ GeV}$ .

## 6 Summary

A search for compressed higgsino and wino dark matter has been performed using events containing a soft, slightly displaced track and large  $p_T^{\text{miss}}$ . A parameterized NN was employed to optimize sensitivity across a wide range of models not previously probed, and no significant excess above the standard model prediction is observed. The resulting 95% confidence level limits exclude chargino masses up to 185 GeV for a mass splitting of 0.55 GeV, as well as mass

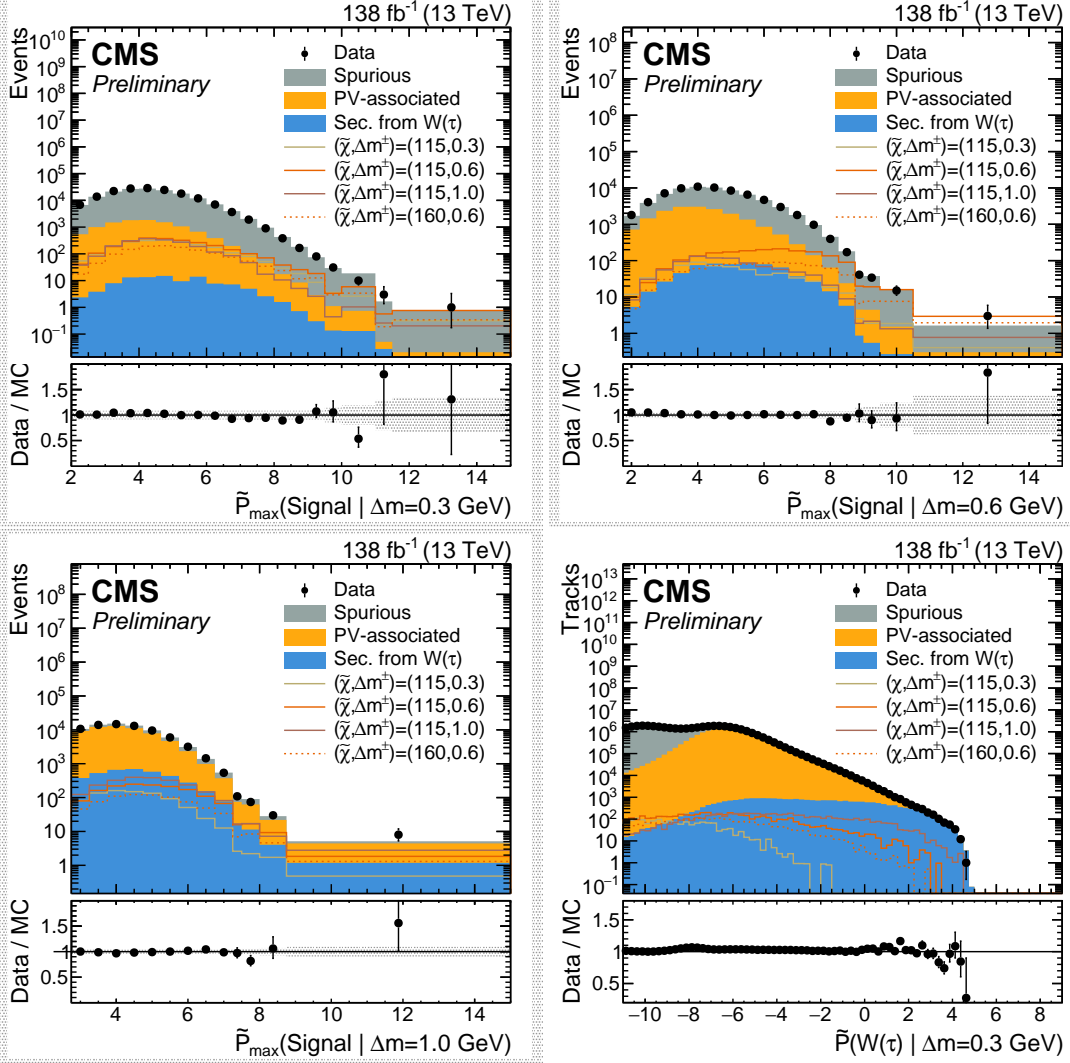


Figure 4: The first three plots show the expected and observed data in the signal-sensitive observables  $\tilde{P}_{\max}(\text{Signal} \mid \Delta m = \{0.3, 0.6, 1.0\} \text{ GeV})$ . In the lower ratio panel, the gray shaded region shows the relative statistical uncertainty in the background estimate, while the black vertical error bars indicate the total uncertainty in each bin. The fourth plot shows the output of the  $\tau$  node of tracks with a loose selection of  $\tilde{P}(\text{Signal} \mid \Delta m = 0.3 \text{ GeV}) > -2$ , indicating the  $\tau$ -based signal proxy region.

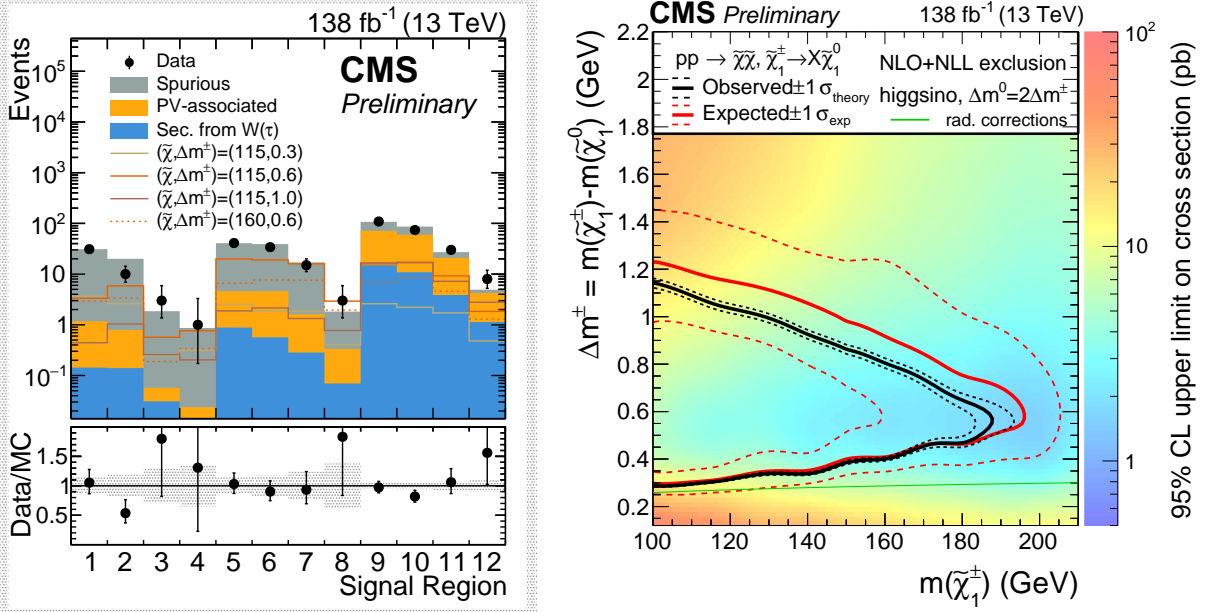


Figure 5: Left: Expected and observed counts in the 12 SRs. The black error bars and gray band in the lower panel show the relative statistical uncertainties in the data and prediction. Four signal benchmark models are shown, corresponding to the inclusive production of all possible pairs of higgsino-like electroweakinos. Right: The heat map shows the 95% CL upper limit on the cross section. The expected (red) and observed (black) bounds indicate the region to the left of which the model space is excluded, assuming theoretical cross sections calculated at NLO-NLL [56, 57]. Red dashed lines show the expected limits varied by the experimental uncertainties while black dashed lines are the observed limits with theoretical cross sections varied by their uncertainty. Branching fractions of the chargino are taken from [58].

splittings of 0.33-1.2 GeV for a 100 GeV higgsino—currently the most stringent constraints in this model space—thereby exerting additional pressure on natural SUSY dark matter scenarios.

## A NN architecture and input variables

The classifier NN has a 3-layer architecture with 256 hidden units, LeakyReLU activations, preprocessing layers for normalization, and categorical cross-entropy loss for training. The variables taken as input to this discriminator are summarized in Table 3. A custom helical extrapolation of the track incorporates the position of the selected PV to improve efficiency for soft and displaced particles, and is used to label simulated tracks with their generator truth particle. Table 4 lists the set of custom track observables defined using the helix extrapolation.

The refiner NN used for the MC shape correction is built with 5 residual blocks, each containing 2 hidden layers with 512 nodes per layer and utilizing the LeakyReLU activation function for non-linear transformations. It is optimized using the Adam optimizer with a learning rate of  $1 \times 10^{-5}$  to minimize the maximum mean discrepancy (MMD) loss, employing kernel bandwidths tailored to key features such as  $\log_{10}(p_T)$ ,  $\log_{10}(dx^{\text{Error}})$ , and  $\log_{10}(dz^{\text{Error}})$ . The model is trained over 2000 epochs on a dataset of 151,552 samples with a batch size of 4096.

Table 3: Variables used by the NN soft track classifier.

Variable	Description
$\Delta m^\pm$	Model mass splitting.
$p_T$	Transverse momentum of the track.
$ \eta $	Pseudorapidity of the track.
$ \Delta\phi(\text{Track}, \vec{p}_T^{\text{miss}}) $	Azimuthal angle between the track and the $p_T^{\text{miss}}$ vector.
$ \Delta\phi(\text{Track}, \text{Leading Jet}) ,$ $ \Delta\eta(\text{Track}, \text{Leading Jet}) $	Azimuthal angle and distance in pseudorapidity between the track and the leading jet.
$\log_{10}(\text{dxy}), \log_{10}(\text{dz})$	Transverse and longitudinal impact parameters (standard straight line approximation) with respect to (a) the leading primary vertex and (b) the closest primary vertex from pileup interactions.
$\log_{10}(\text{dxy}^{\text{Error}}), \log_{10}(\text{dz}^{\text{Error}})$	Error on the transverse and longitudinal impact parameters (standard straight line approximation).
$\log_{10}(\text{IPxy}), \log_{10}(\text{IPz}),$ $\log_{10}(\text{IPxy Significance}),$ $\log_{10}(\text{IPz Significance})$	Transverse and longitudinal impact parameters and impact parameter significances (custom helix extrapolation) with respect to (a) the leading primary vertex, (b) the closest primary vertex from pileup interactions, (c) the primary vertex associated to the track during reconstruction, and (d) the closest primary vertex excluding the associated vertex.
$\Delta\text{xy}(\text{PV}, \text{ass. PV}),$ $\Delta\text{z}(\text{PV}, \text{ass. PV})$	Distance in the transverse plane and along the z-axis between the leading primary vertex and the primary vertex associated to the track (if assigned).
$\Delta\text{xy}(\text{PV}, \text{ass. SV}),$ $\Delta\text{z}(\text{PV}, \text{ass. SV})$	Distance in the transverse plane and along the z-axis between the leading primary vertex and the secondary vertex associated to the track (if assigned).
Abs. Iso PF	Sum of transverse momenta of PF candidates within a cone of $\Delta R < 0.3$ around the track.
$\Delta R_{\text{min}}$	Distances to the (a) closest jet with $p_T > 30 \text{ GeV}$ , (b) closest jet with $p_T > 15 \text{ GeV}$ , (c) closest track with $p_T > 5 \text{ GeV}$ , and (d) second closest track with $p_T > 5 \text{ GeV}$ .
$p_T^{\text{miss}}$	Event-level magnitude of $p_T^{\text{miss}}$ .

Table 4: Custom track observables defined using the track helix extrapolation. All quantities are defined with respect to (a) the leading PV, (b) the closest PV from pileup interactions, (c) the PV associated to the track during reconstruction, and (d) the closest PV excluding the associated vertex.

Observable	Description
IP	Distance in 3D (impact parameter) between a track and a vertex, evaluated at the point of closest approach in 3D between the track helix and the vertex.
IP Significance	Impact parameter significance, $IP/\sigma(IP)$ , with uncertainty $\sigma(IP)$ computed by propagating the covariance matrices of the track and the vertex.
IP <sub>xy</sub>	Distance in the transverse plane (transverse impact parameter) between a track and a vertex, evaluated at the point of closest approach in 3D between the track helix and the vertex.
IP <sub>xy</sub> Significance	Transverse impact parameter significance, $IP_{xy}/\sigma(IP_{xy})$ , with uncertainty $\sigma(IP_{xy})$ computed by propagating the covariance matrices of the track and the vertex.
IP <sub>z</sub>	Distance along the z-axis (longitudinal impact parameter) between a track and the PV, evaluated at the point of closest approach in 3D between the track helix and the PV.
IP <sub>z</sub> Significance	Transverse impact parameter significance, $IP_z/\sigma(IP_z)$ , with uncertainty $\sigma(IP_z)$ computed by propagating the covariance matrices of the track and the vertex.

## References

- [1] P. Ramond, “Dual theory for free fermions”, *Phys. Rev. D* **3** (1971) 2415, doi:10.1103/PhysRevD.3.2415.
- [2] Y. A. Gol’fand and E. P. Likhtman, “Extension of the algebra of Poincaré group generators and violation of P invariance”, *JETP Lett.* **13** (1971) 323.
- [3] A. Neveu and J. H. Schwarz, “Factorizable dual model of pions”, *Nucl. Phys. B* **31** (1971) 86, doi:10.1016/0550-3213(71)90448-2.
- [4] D. V. Volkov and V. P. Akulov, “Possible universal neutrino interaction”, *JETP Lett.* **16** (1972) 438.
- [5] J. Wess and B. Zumino, “A Lagrangian model invariant under supergauge transformations”, *Phys. Lett. B* **49** (1974) 52, doi:10.1016/0370-2693(74)90578-4.
- [6] J. Wess and B. Zumino, “Supergauge transformations in four dimensions”, *Nucl. Phys. B* **70** (1974) 39, doi:10.1016/0550-3213(74)90355-1.
- [7] P. Fayet, “Supergauge invariant extension of the Higgs mechanism and a model for the electron and its neutrino”, *Nucl. Phys. B* **90** (1975) 104, doi:10.1016/0550-3213(75)90636-7.
- [8] P. Fayet and S. Ferrara, “Supersymmetry”, *Phys. Rept.* **32** (1977) 249, doi:10.1016/0370-1573(77)90066-7.

- [9] H. P. Nilles, “Supersymmetry, supergravity and particle physics”, *Phys. Rep.* **110** (1984) 1, doi:10.1016/0370-1573(84)90008-5.
- [10] F. Zwicky, “On the masses of nebulae and of clusters of nebulae”, *Astrophys. J.* **86** (1937) 217, doi:10.1086/143864.
- [11] V. C. Rubin and W. K. Ford, Jr., “Rotation of the Andromeda nebula from a spectroscopic survey of emission regions”, *Astrophys. J.* **159** (1970) 379, doi:10.1086/150317.
- [12] R. Barbieri and G. F. Giudice, “Upper bounds on supersymmetric particle masses”, *Nuclear Physics B* **306** (1988), no. 1, 63, doi:10.1016/0550-3213(88)90171-X.
- [13] S. P. Martin, “A supersymmetry primer”, *Adv. Ser. Direct. High Energy Phys.* **18** (1998) 1, doi:10.1142/9789812839657\_0001, arXiv:hep-ph/9709356.
- [14] Planck Collaboration, “Planck 2018 results. VI. Cosmological parameters”, *Astron. Astrophys.* **641** (2020) A6, doi:10.1051/0004-6361/201833910, arXiv:1807.06209. [Erratum: doi:10.1051/0004-6361/201833910e].
- [15] ATLAS Collaboration, “The ATLAS experiment at the CERN Large Hadron Collider”, *JINST* **3** (2008) S08003, doi:10.1088/1748-0221/3/08/S08003.
- [16] CMS Collaboration, “The CMS experiment at the CERN LHC”, *JINST* **3** (2008) S08004, doi:10.1088/1748-0221/3/08/S08004.
- [17] LZ Collaboration, “First Dark Matter Search Results from the LUX-ZEPLIN (LZ) Experiment”, *Phys. Rev. Lett.* **131** (2023), no. 4, 041002, doi:10.1103/PhysRevLett.131.041002, arXiv:2207.03764.
- [18] XENON100 Collaboration, “XENON100 Dark Matter Results from a Combination of 477 Live Days”, *Phys. Rev. D* **94** (2016), no. 12, 122001, doi:10.1103/PhysRevD.94.122001, arXiv:1609.06154.
- [19] PandaX Collaboration, “First dark matter search results from the PandaX-I experiment”, *Sci. China Phys. Mech. Astron.* **57** (2014) 2024, doi:10.1007/s11433-014-5598-7, arXiv:1408.5114.
- [20] CMS Collaboration, “Phenomenological MSSM interpretation of CMS searches in pp collisions at 13 TeV”, technical report, CERN, Geneva, 2024.
- [21] N. Nagata and S. Shirai, “Higgsino Dark Matter in High-Scale Supersymmetry”, *JHEP* **01** (2015) 029, doi:10.1007/JHEP01(2015)029, arXiv:1410.4549.
- [22] ATLAS Collaboration, “Searches for electroweak production of supersymmetric particles with compressed mass spectra in  $\sqrt{s} = 13$  TeV  $pp$  collisions with the ATLAS detector”, *Phys. Rev. D* **101** (2020), no. 5, 052005, doi:10.1103/PhysRevD.101.052005, arXiv:1911.12606.
- [23] CMS Collaboration, “Search for supersymmetry in final states with two or three soft leptons and missing transverse momentum in proton-proton collisions at  $\sqrt{s} = 13$  TeV”, *JHEP* **04** (2022) 091, doi:10.1007/JHEP04(2022)091, arXiv:2111.06296.
- [24] CMS Collaboration, “Search for disappearing tracks in proton-proton collisions at  $\sqrt{s} = 13$  TeV”, *Phys. Lett. B* **806** (2020) 135502, doi:10.1016/j.physletb.2020.135502, arXiv:2004.05153.

- 
- [25] ATLAS Collaboration, “Search for long-lived charginos based on a disappearing-track signature using  $136 \text{ fb}^{-1}$  of  $pp$  collisions at  $\sqrt{s} = 13 \text{ TeV}$  with the ATLAS detector”, technical report, CERN, Geneva, 2021. All figures including auxiliary figures are available at <https://atlas.web.cern.ch/Atlas/GROUPS/PHYSICS/CONFNOTES/ATLAS-CONF-2021-015>.
- [26] CMS Collaboration, “Search for supersymmetry in final states with disappearing tracks in proton-proton collisions at  $\sqrt{s} = 13 \text{ TeV}$ ”, *Phys. Rev. D* **109** (2024), no. 7, 072007, doi:10.1103/PhysRevD.109.072007, arXiv:2309.16823.
- [27] ATLAS Collaboration, “Search for nearly mass-degenerate higgsinos using low-momentum mildly-displaced tracks in  $pp$  collisions at  $\sqrt{s} = 13 \text{ TeV}$  with the ATLAS detector”, *Phys. Rev. Lett.* **132** (2024), no. 22, 221801, doi:10.1103/PhysRevLett.132.221801, arXiv:2401.14046.
- [28] CMS Tracker Group Collaboration, “The CMS phase-1 pixel detector upgrade”, *JINST* **16** (2021) P02027, doi:10.1088/1748-0221/16/02/P02027, arXiv:2012.14304.
- [29] CMS Collaboration, “Particle-flow reconstruction and global event description with the CMS detector”, *JINST* **12** (2017) P10003, doi:10.1088/1748-0221/12/10/P10003, arXiv:1706.04965.
- [30] CMS Collaboration, “Technical proposal for the Phase-II upgrade of the Compact Muon Solenoid”, CMS Technical Proposal CERN-LHCC-2015-010, CMS-TDR-15-02, 2015.
- [31] M. Cacciari, G. P. Salam, and G. Soyez, “The anti- $k_T$  jet clustering algorithm”, *JHEP* **04** (2008) 063, doi:10.1088/1126-6708/2008/04/063, arXiv:0802.1189.
- [32] M. Cacciari, G. P. Salam, and G. Soyez, “FastJet user manual”, *Eur. Phys. J. C* **72** (2012) 1896, doi:10.1140/epjc/s10052-012-1896-2, arXiv:1111.6097.
- [33] CMS Collaboration, “Jet performance in  $pp$  collisions at  $\sqrt{s} = 7 \text{ TeV}$ ”, CMS Physics Analysis Summary CMS-PAS-JME-10-003, 2010.
- [34] CMS Collaboration, “Jet algorithms performance in 13 TeV data”, CMS Physics Analysis Summary CMS-PAS-JME-16-003, 2017.
- [35] CMS Collaboration, “Jet energy scale and resolution in the CMS experiment in  $pp$  collisions at 8 TeV”, *JINST* **12** (2017) P02014, doi:10.1088/1748-0221/12/02/P02014, arXiv:1607.03663.
- [36] M. Cacciari and G. P. Salam, “Pileup subtraction using jet areas”, *Phys. Lett. B* **659** (2008) 119, doi:10.1016/j.physletb.2007.09.077, arXiv:0707.1378.
- [37] CMS Collaboration, “Identification of heavy-flavour jets with the CMS detector in  $pp$  collisions at 13 TeV”, *JINST* **13** (2018) P05011, doi:10.1088/1748-0221/13/05/P05011, arXiv:1712.07158.
- [38] J. Alwall et al., “The automated computation of tree-level and next-to-leading order differential cross sections, and their matching to parton shower simulations”, *JHEP* **07** (2014) 079, doi:10.1007/JHEP07(2014)079, arXiv:1405.0301.

- [39] J. Alwall et al., “Comparative study of various algorithms for the merging of parton showers and matrix elements in hadronic collisions”, *Eur. Phys. J. C* **53** (2008) 473, doi:10.1140/epjc/s10052-007-0490-5, arXiv:0706.2569.
- [40] GEANT4 Collaboration, “GEANT4—a simulation toolkit”, *Nucl. Instrum. Meth. A* **506** (2003) 250, doi:10.1016/S0168-9002(03)01368-8.
- [41] CMS Collaboration, “Event generator tunes obtained from underlying event and multiparton scattering measurements”, *Eur. Phys. J. C* **76** (2016) 155, doi:10.1140/epjc/s10052-016-3988-x, arXiv:1512.00815.
- [42] CMS Collaboration, “Extraction and validation of a new set of CMS PYTHIA8 tunes from underlying-event measurements”, *Eur. Phys. J. C* **80** (2020) 4, doi:10.1140/epjc/s10052-019-7499-4, arXiv:1903.12179.
- [43] NNPDF Collaboration, “Parton distributions with QED corrections”, *Nucl. Phys. B* **877** (2013) 290, doi:10.1016/j.nuclphysb.2013.10.010, arXiv:1308.0598.
- [44] NNPDF Collaboration, “Parton distributions from high-precision collider data”, *Eur. Phys. J. C* **77** (2017) 663, doi:10.1140/epjc/s10052-017-5199-5, arXiv:1706.00428.
- [45] T. Sjöstrand et al., “An Introduction to PYTHIA 8.2”, *Comput. Phys. Commun.* **191** (2015) 159, doi:10.1016/j.cpc.2015.01.024, arXiv:1410.3012.
- [46] S. Abdullin et al., “The fast simulation of the CMS detector at LHC”, *J. Phys. Conf. Ser.* **331** (2011) 032049, doi:10.1088/1742-6596/331/3/032049.
- [47] A. Giammanco, “The fast simulation of the CMS experiment”, *J. Phys. Conf. Ser.* **513** (2014) 022012, doi:10.1088/1742-6596/513/2/022012.
- [48] R. Mahbubani, P. Schwaller, and J. Zurita, “Closing the window for compressed Dark Sectors with disappearing charged tracks”, *JHEP* **06** (2017) 119, doi:10.1007/JHEP06(2017)119, arXiv:1703.05327. [Erratum: *JHEP* 10, 061 (2017)].
- [49] CMS Collaboration, “Performance of missing transverse momentum reconstruction in proton-proton collisions at  $\sqrt{s} = 13$  TeV using the CMS detector”, 2019. arXiv:1903.06078. Accepted by *JINST*.
- [50] A. Gretton et al., “A kernel two-sample test”, *Journal of Machine Learning Research* **13** (2012), no. 25, 723.
- [51] M. Wolf et al., “Fast Perfekt: Regression-based refinement of fast simulation”, *SciPost Phys. Core* **8** (2025) 021, doi:10.21468/SciPostPhysCore.8.1.021.
- [52] CMS Collaboration, “Precision luminosity measurement in proton-proton collisions at  $\sqrt{s} = 13$  TeV in 2015 and 2016 at CMS”, *Eur. Phys. J. C* **81** (2021) 800, doi:10.1140/epjc/s10052-021-09538-2, arXiv:2104.01927.
- [53] CMS Collaboration, “CMS luminosity measurement for the 2017 data-taking period at  $\sqrt{s} = 13$  TeV”, CMS Physics Analysis Summary CMS-PAS-LUM-17-004, 2018.
- [54] CMS Collaboration, “CMS luminosity measurement for the 2018 data-taking period at  $\sqrt{s} = 13$  TeV”, CMS Physics Analysis Summary CMS-PAS-LUM-18-002, 2019.

- [55] A. Giraldi, "Precision luminosity measurement with proton-proton collisions at the CMS experiment in Run 2", in *Proc. 41st Int. Conf. on High Energy Physics (ICHEP2022)*, p. 638. 2022. arXiv:2208.08214. [PoS(ICHEP2022)638]. doi:10.22323/1.414.0638.
- [56] B. Fuks, M. Klasen, D. R. Lamprea, and M. Rothering, "Gaugino production in proton-proton collisions at a center-of-mass energy of 8 TeV", *JHEP* **10** (2012) 081, doi:10.1007/JHEP10(2012)081, arXiv:1207.2159.
- [57] B. Fuks, M. Klasen, D. R. Lamprea, and M. Rothering, "Precision predictions for electroweak superpartner production at hadron colliders with RESUMMINO", *Eur. Phys. J. C* **73** (2013) 2480, doi:10.1140/epjc/s10052-013-2480-0, arXiv:1304.0790.
- [58] M. Ibe, Y. Nakayama, and S. Shirai, "Precise estimate of charged Higgsino/Wino decay rate", *JHEP* **03** (2024) 012, doi:10.1007/JHEP03(2024)012, arXiv:2312.08087.